Geomechanics and Engineering, *Vol. 20, No. 5 (2020) 461-474*
DOI: https://doi.org/10.12989/gae.2020.20.5.461

Incompatible deformation and damage evolution of mixed strata specimens containing a circular hole

Shuo Yang[1], Yuanhai Li[*1,2], Miao Chen[3] and Jinshan Liu[1,2]

[1]*State Key Laboratory for Geomechanics and Deep Underground Engineering, China University of Mining and Technology, Xuzhou 221116, China*
[2]*School of Mechanics and Civil Engineering, China University of Mining and Technology, Xuzhou 221116, China*
[3]*State Key Laboratory of Mine Disaster Prevention and Control, Shandong University of Science and Technology, Qingdao 266590, China*

(Received December 24, 2019, Revised February 9, 2020, Accepted February 12, 2020)

Abstract. Analysing the incompatible deformation and damage evolution around the tunnels in mixed strata is significant for evaluating the tunnel stability, as well as the interaction between the support system and the surrounding rock mass. To investigate this issue, confined compression tests were conducted on upper-soft and lower-hard strata specimens containing a circular hole using a rock testing system, the physical mechanical properties were then investigated. Then, the incompatible deformation and failure modes of the specimens were analysed based on the digital speckle correlation method (DSCM) and Acoustic Emission (AE) data. Finally, numerical simulations were conducted to explore the damage evolution of the mixed strata. The results indicate that at low inclination angles, the deformation and v-shaped notches inside the hole are controlled by the structure plane. Progressive spalling failure occurs at the sidewalls along the structure plane in soft rock. But the transmission of the loading force between the soft rock and hard rock are different in local. At high inclination angles, v-shaped notches are approximately perpendicular to the structure plane, and the soft and hard rock bear common loads. Incompatible deformation between the soft rock and hard rock controls the failure process. At inclination angles of 0°, 30° and 90°, incompatible deformations are closely related to rock damage. At 60°, incompatible deformations and rock damage are discordant that the soft rock and hard rock alternately bears the major loads during the failure process. The failure trend and modes of the numerical results agree very well with those observed in the experimental results. As the inclination angles increase, the proportion of the shear or tensile damage exhibits a nonlinear increase or decrease, suggesting that the inclination angle of mixed strata may promote shear damage and restrain tensile damage.

Keywords: circular hole; mixed strata; incompatible deformation; damage evolution; failure mode

1. Introduction

Mixed strata are commonly encountered during tunnel construction, and may cause many challenges and pose a great threat to security, with issues such as TBM (tunnel boring machine) jamming and support failure (Mezger *et al*. 2017, Zang *et al*. 2020). Mixed strata are characterized by the simultaneous presence of two or more geological materials on the tunnel face that exhibit intrinsic discontinuities or structural anisotropy (Tóth *et al*. 2013). The mechanical properties of mixed strata normally appear to be approximately the same when the strata are parallel to the bedding direction, and a great difference is normally observed in the vertical direction. The configuration of the rock strata affects the mechanical behaviour of the rock mass and the failure mode of the tunnel (Wang *et al*. 2012). The angles between the direction of tunnelling and the rock formations are also a predominant influence factor. An analysis of the incompatible deformation and damage evolution around the tunnels in mixed strata are significant for evaluating of the tunnel stability, as well as the interaction between the support system and the surrounding rock mass.

As a type of mixed strata, transversely isotropic rock (Fig. 1(a)) has been widely investigated. Transversely isotropic rocks, such as sedimentary rocks, are characterized by obviously bedded and anisotropy structures. Tien *et al*. (2006) investigated the failure process and failure modes of transversely isotropic rock and found that it has three failure modes: tensile fracture across the discontinuities, tensile-split along the discontinuities, and sliding failure across the discontinuities. Cheng *et al*. (2017) studied the anisotropy of the strength and deformation of the composite rock under uniaxial loading and concluded that when the anisotropic angle θ increased from 0° to 90°, the peak strength, peak strain, and apparent elastic modulus all initially decreased and then increased. Yang *et al*. (2019b) employed X-ray computed tomography (CT) scanning to investigate the failure mechanism of transversely isotropic composite rock under different confining pressures and found that the deformation of specimens is incompatible, the failure behaviour mostly depends on the angle between the loading direction and the discontinuity plane.

Layered rock masses with transversely isotropic structures have also been investigated in previous studies (Berčáková *et al*. 2019, Chen *et al*. 2019c, Cho *et al*. 2012,

∗Corresponding author, Professor
E-mail: Lyh@cumt.edu.cn

ISSN: 2005-307X (Print), 2092-6219 (Online)

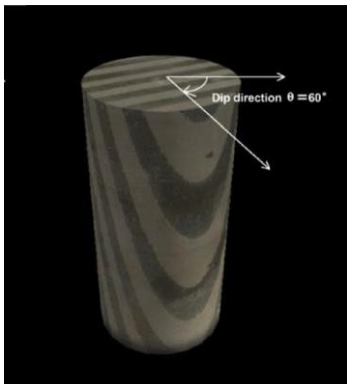

(a) Transversely isotropic rocks (Tien *et al*. 2006)

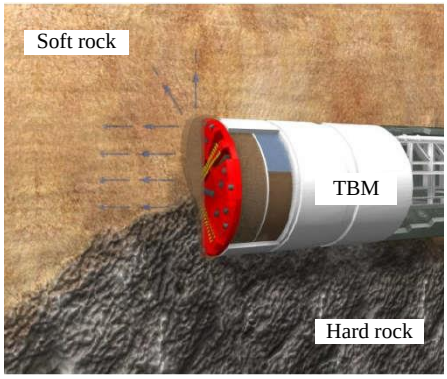

(b) Upper-soft and lower-hard strata encountered in tunnel excavation (Cheng 2018)

Fig. 1 Types of mixed strata

Dutler *et al*. 2018, Fortsakis *et al*. 2012, Li *et al*. 2019a, Lisjak *et al*. 2015, Wang *et al*. 2019a, Wang *et al*. 2019b). These studies concluded that with an increase in the inclination angles, the AE counts show evident anisotropy and are associated with shearing. Failure initiates due to shearing of the bedding planes, and parts of the internal rock mass obviously behave as a beam. Slippage-induced rock masses promote extensional fracturing in the direction perpendicular to the bedding orientation. The asymmetric effect of the deformation mechanism is mainly controlled by the inclination angle of the rock layer and the shear stress. Rock-concrete (Dong *et al*. 2019, Dong *et al*. 2017, Selçuk and Aşma, 2019, Zhong *et al*. 2014) and rock-coal (Chen *et al*. 2019a, Chen *et al*. 2019b, Cheng *et al*. 2019a, Cheng *et al*. 2019b) specimens that have similar structures have been well studied. These studies focus on the nonlinear fracture characteristics of the interface. Although the above studies have provided many valuable results, the incompatible deformation and damage evolution around circular tunnels still remain limited and require further investigation.

Furthermore, limited laboratory experiments have been conducted on upper-soft and lower-hard strata containing circular tunnels (Fig. 1(b)). It is rather difficult or even impossible to obtain natural rock with upper-soft and lower-hard layers for research. Rock-like specimens were thus chosen as alternative options. Yang *et al*. (2018) investigated the effect of soft and hard strata on the stability of rock surrounding tunnels through physical experiments and numerical simulations and found that the final failure model shows obvious asymmetrical deformation. The soft rock area experiences block dropping and roof falling, while the hard rock only shows shrinkage deformation. Gong *et al*. (2015) studied the process of tunnel instability in horizontal mixed strata to investigate its nonlinear behaviour. These above laboratory studies ignored the interaction between the laminated layers due to the limitation of testing materials. The shearing process between the interface influences the failure modes of specimens (Liu *et al*. 2020a, b). Furthermore, Duan *et al*. (2019) found that the degree of cementation at the interface of composite rock specimens has a little effect on strength, but has a significant impact on the failure modes. Thus, the degree of cementation at the interface of mixed strata should be particularly concerned.

Despite recent progress, the incompatible deformation and damage evolution of the tunnels in upper-soft and lower-hard strata remain to be elucidated. In this study, confined compression tests were conducted on upper-soft and lower-hard strata specimens containing a circular hole using a rock testing system, which has concerned the degree of cementation at the interface. The physical mechanical properties were then investigated. Then, the incompatible deformation and failure modes of the specimens were analysed based on the DSCM and AE data. Finally, numerical simulations were conducted to explore the damage evolution of the mixed strata.

2. Experimental materials and test procedure

2.1 Experimental materials and specimen preparation

In this research, upper-soft and lower-hard strata specimens were composed of mudstone and sandstone, which are commonly encountered during tunnel construction. The sandstone and mudstone used in this research were collected from Renshou city, Sichuan province of China. As shown in Table 1, according to the X-ray diffraction (XRD) analysis, the mineral types and components of the tested specimens were obtained. By using scanning electron microscopy (SEM), as seen in Fig. 2(a) and (b), the mineral particles of the mudstone samples were in loose connection with many larger cracks and pores. In contrast, mineral grains of the sandstone samples were cemented closely, and few cracks and pores can be observed. The diverse microstructural characteristics result in differences in the mechanical parameters (Zhang *et al*. 2019a, b, c), which are listed in Table 2.

The rock specimens were all machined at the same direction from the same block of rock material. Then, the surfaces of the specimen were ground to produce flat surfaces in order to maintain a uniform load distribution. Due to a large difficulty of obtaining natural rock with upper-soft and lower-hard layers, the mixed strata specimens in this study were cemented by mudstone and

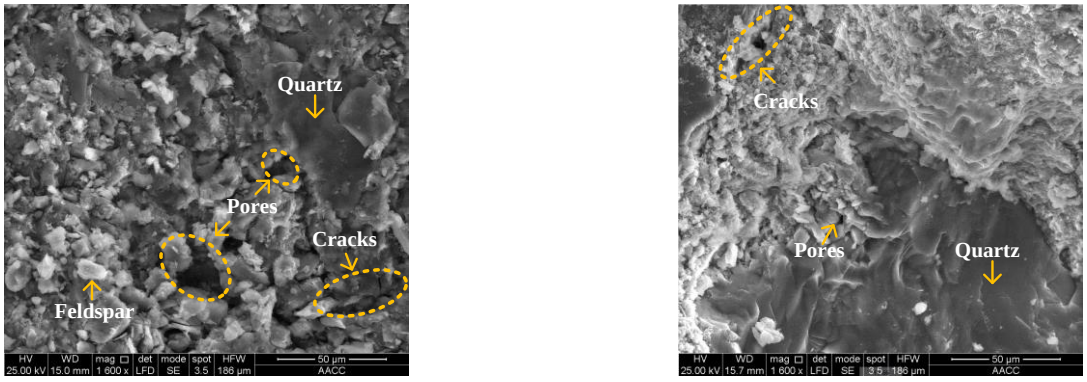

(a) Mudstone (b) Sandstone

Fig. 2 SEM images of test specimens

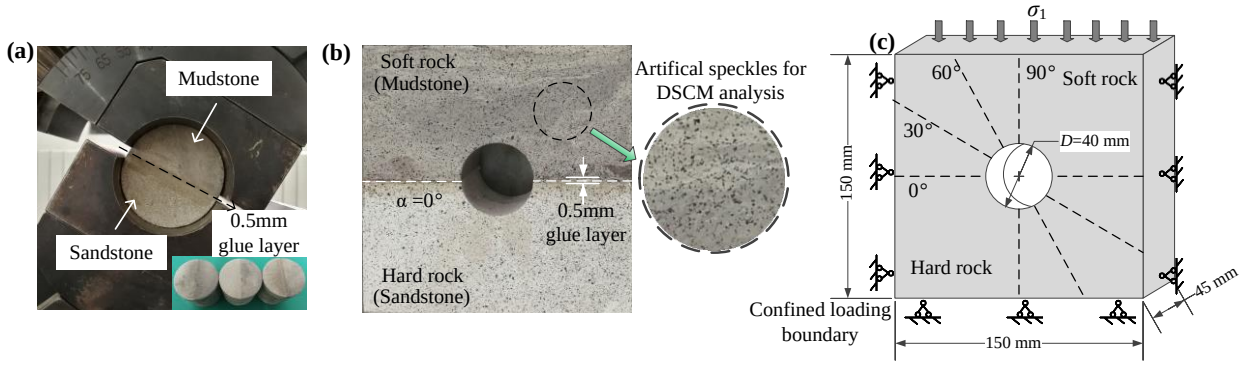

Fig. 3 Specimen preparation. (a) Variable angle shear test of the structure planes in the mixed strata, (b) Artificial speckles for DSCM and (c) Load mode of specimens

Table 1 Mineral types and components of mixed strata specimens

Lithology	Quartz (%)	Feldspar (%)	Siderite (%)	Calcite (%)	Clay minerals (%)
Mudstone	49.3	16.3	0.9	-	33.5
Sandstone	82.8	3.1	0.9	0.2	13.0

Table 2 Basic mechanical parameters of the mixed strata specimens

Lithology	Uniaxial compressive strength (MPa)	Tensile strength (MPa)	Cohesion (MPa)	Internal friction angle (°)	Elastic modulus (GPa)	Poisson's ratio
Mudstone	12.23	1.48	2.57	34	1.50	0.30
Sandstone	45.86	3.31	7.92	45	5.97	0.24

sandstone plate specimens. The structure planes of the mixed strata were cemented by stone glue with a 0.5 mm thick glue layer. As shown in Fig. 3(a), mechanical properties tests of the structure planes for mixed strata were conducted to simulate the natural structure planes in situ (Meng *et al*. 2009). The test cohesion value (0.15 MPa) was close to the value in situ (0.1 MPa).

The same manufacturing methods for mixed strata were applied to the square plate specimen with a hole, as shown in Fig. 3(b). Then, artificial speckles were sprayed on the surface of the specimen for the DSCM analysis.

The pre-existing hole has a strength-scale effect (Martin, 1997), and its influence increases with a decreasing diameter. Further, the excavation influence is more than three times that of the tunnel diameter. All things considered, each specimen has a pre-existing hole with a diameter of 40 mm machined by water drilling, the dimensions of the specimens were 150 mm wide, 150 mm high and 45 mm thick. As shown in Fig. 3(c). Strata dip angles were varied from 0° to 90° at intervals of 30°.

2.2 Testing system

As shown in Fig. 4, the testing system comprised an MTS816 rock mechanics servo-controlled testing system, a DSCM measuring system, and an AE monitoring system. To simulate the boundary of the surrounding rock (Fig. 3(c)), the sample was clamped by two rigid steel blocks. Petroleum jelly was applied around the specimen interface to decrease the effect of platen restraint and end friction. All experiments were conducted at the State Key Laboratory for Geomechanics and Deep Underground Engineering, China University of Mining and Technology.

Acoustic emission equipment was applied to record the rock failure moment during the loading process. Two AE sensors were attached to the back of the specimen near the hole, adopting a hot bar as a coupler and affixed with tapes (Fig. 4(b)). The acoustic emission signals were recorded in full waveform during the test with the setting threshold at 45 dB and a preamplifier at 40 dB.

The surface failure process of the specimen was captured by a Charge-Coupled Device(CCD) camera at a

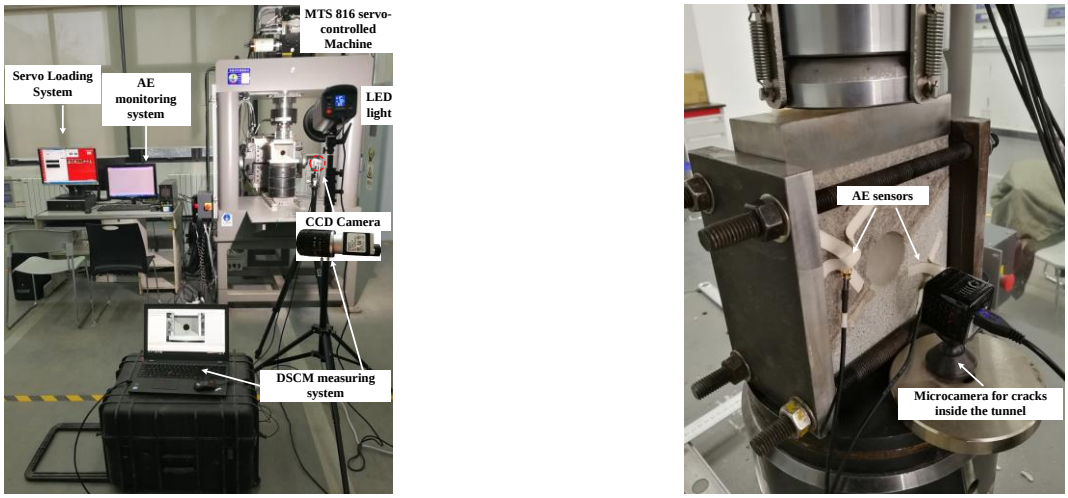

(a) Front view of the experimental system (b) Rear view of the specimen

Fig. 4 Arrangement of the physical model experiment

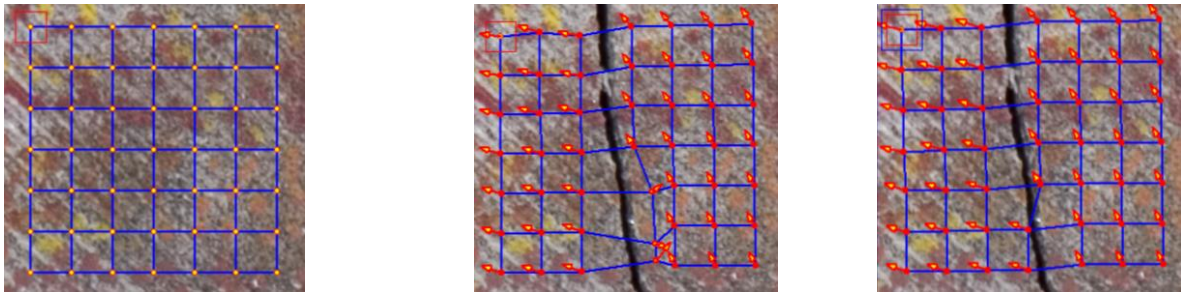

(a) Before fracture (b) Original algorithm (c) OPFPM algorithm

Fig. 5 Comparison of the measurement precision with the OPFPM

rate of 8 frames per second. The captured rock-surface images were analysed by the DSCM self-developed software- PhotoInfor. The accuracies of the measurements in PhotoInfor have been proven based on both a theoretical analysis and experimental tests (Li *et al*. 2019b). Relative sensitivity (0.058 mm/ pixel) was determined by a special calibration calculated by calibration distance (unit: mm) and speckle image distance (unit: pixel). The analysis grid contained 1281 blocks with 48 pixels between two measuring points. Subset radius and searching radius were set to 1 and 15 pixels respectively. Furthermore, a microcamera was placed behind the specimen to record the failure process of the hole sidewalls under the loading condition in real-time.

One point and five pixel blocks method (OPFPM) (Li *et al*. 2016) of PhotoInfor was used to measure the large deformation while cracks appear. This method avoids the low image correlation caused by cracks. Therefore, the misjudgement of image pixels is reduced, and the large deformation analysis accuracy is improved. The OPFPM algorithm finds a pixel block not crossing the crack that can avoid low image correlation caused by the fracture. As shown in Fig. 5, obvious mistakes appear in the fracture zones with the original methods, whereas excellent results are achieved with the OPFPM algorithm. Therefore, the OPFPM algorithm provides higher accuracy for studying large deformation along with cracks.

2.3 Testing procedures

Before the test, the bolts were tightened with the same known torque to apply small initial horizontal stresses on the two sides of the specimen. Then, the axial force was imposed on the rock specimen surface under displacement-controlled conditions with a strain rate of 0.1 mm/min until failure occurred. The loads and deformations of the specimens were recorded simultaneously at a data collection interval of 1 s.

3. Results of experiment

3.1 AE behaviour and mechanical properties

Fig. 6 shows the AE evolution of the mixed strata containing a circle hole. The variation in the AE counts and the accumulated counts (threshold 45 dB) with respect to the loading time were investigated. At the beginning of loading, with an increase in the inclination angles, the rate of increase is reduced. In this period, the hard rocks support the structure of the specimen, and less micro-cracks occur at the high inclination specimens.

From the inclination angles of 0° to 60°, a maximum AE count corresponds to final failure; however, it also occurs at the peak strength at 90°. This result could be explained by

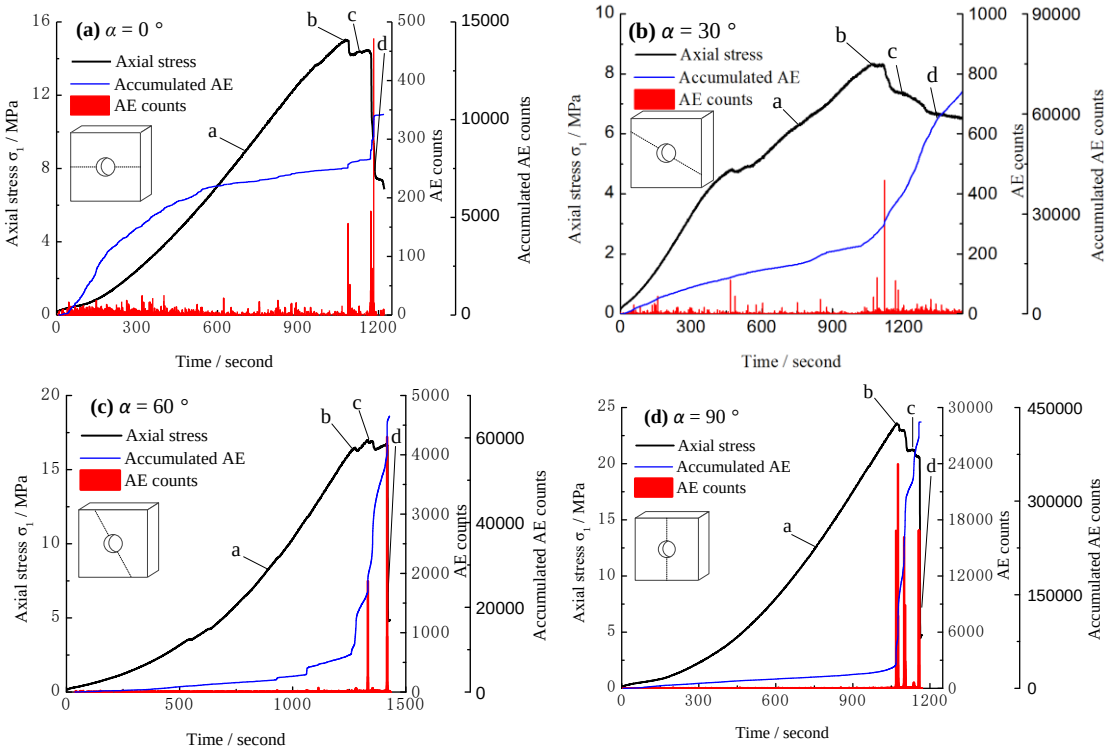

Fig. 6 Stress-time-AE count curves of the mixed strata containing a circle hole

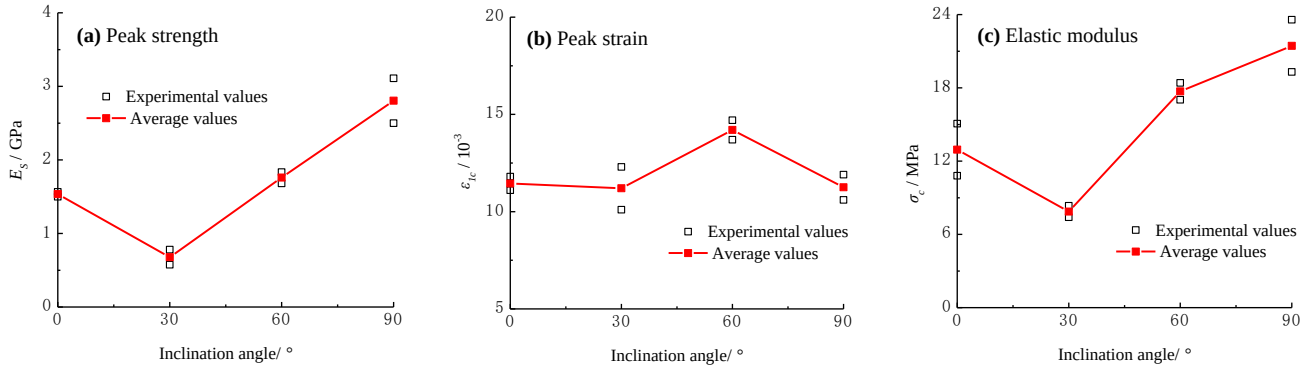

Fig. 7 Effect of the inclination angle on the strength and deformation parameters

considering that low inclination specimens release more energies by crack initiation and propagation at pre-peak stage.

For the nearby post-peak strength, the AE events are most active for each sample. Distinct AE columns are clearly observed, which indicates crack propagation. High inclination specimens have relative high AE counts. As the inclination angles increase, the specimens change from ductile failure to brittle failure.

Fig. 7 shows the effect of the inclination angle on the strength and deformation parameters. To obtain the best possible results, we conducted two experiments at each inclination angle. Both peak strength and elastic modulus of the specimens first decreases and then increases with increasing inclination angle, which shows the "V" type variations with the inclination angle. The minimum and maximum values are at 30° and 90°, respectively. The peak strain shows a different trend that is slightly affected by the inclination angle, except for 60°. This trend is similar to those of experimental studies where the strength anisotropy is greater than the deformation anisotropy (Cho *et al*. 2012). At 60°, the soft rock dominates the deformation at the pre-peak stage, while hard rock dominates the deformation at post-peak stage. A specimen of 60° has the most complicated fracture characteristics, which is further analyzed in the following section.

3.2 Deformation and failure process

Fig. 8 shows deformation evolution of the mixed strata specimens based on the DSCM in confined compression tests, and the colour gamut represents the displacement magnitude. The deformation fields reflect the failure process during the tests.

At an inclination angle of 0° (Fig. 8(a)), soft rock dominates the deformation, which shows a funnel-shape because the circle hole results in a heterogeneous force distribution. When the specimen is loaded to point b, crack

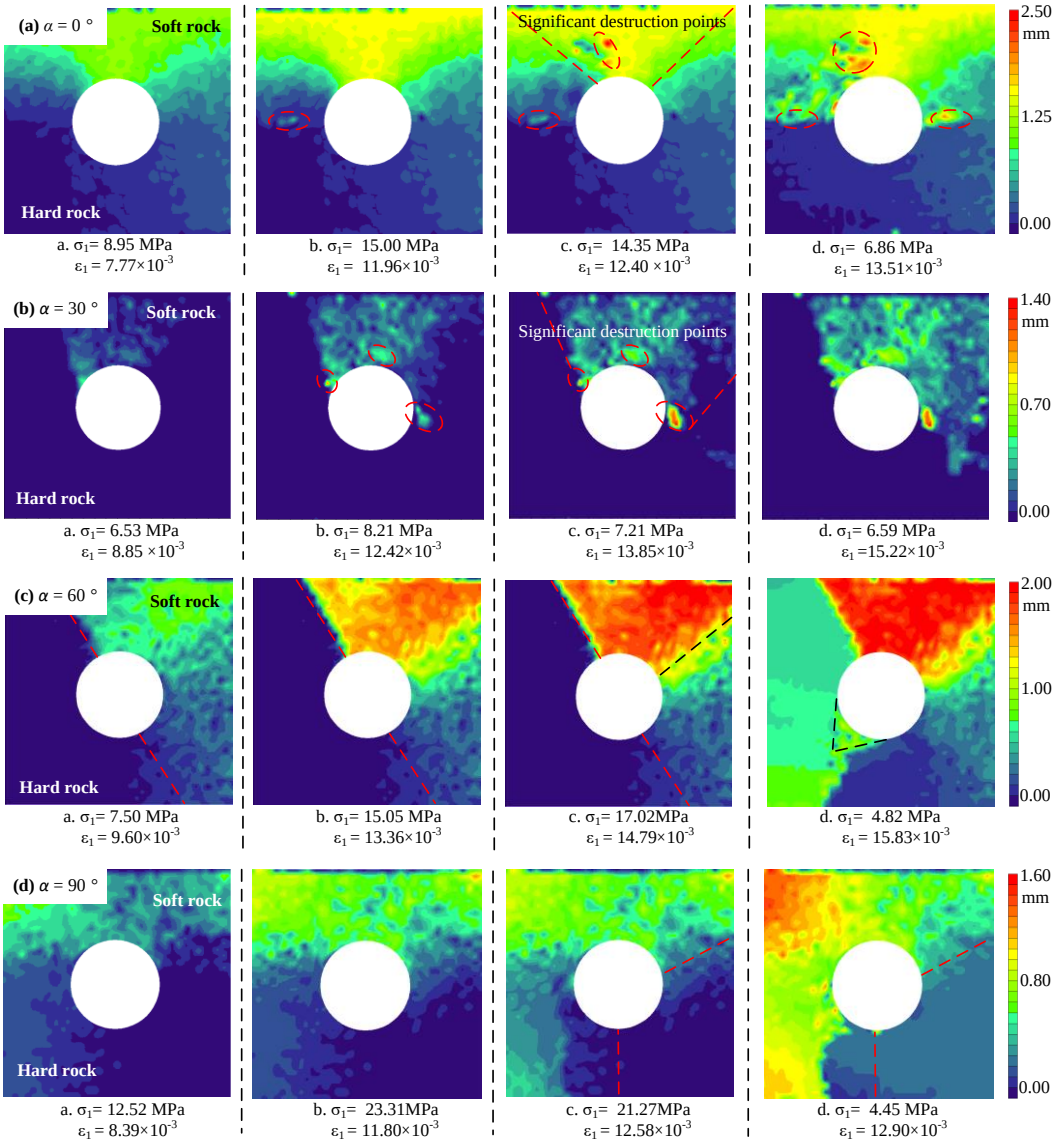

Fig. 8 Deformation evolution of the mixed strata specimens based on the DSCM in confined compression tests corresponding to points (a)-(d) in Fig. 6

initiation occurs on the left of the structure plane. The crack does not simultaneously occur on the right side due to the difficulty of achieving an absolutely uniform material and a uniform loading. As shown in Fig. 9(a), four points located 10 mm away from the hole (roof, two sidewalls, floor) were used to plot the time-deformation curves during the loading process. With continuous vertical loading (point d), roof destruction points begin to occur. Moreover, deformation around the tunnel changes due to stress redistribution. At the post-peak stage (point d), the cracks mainly propagate at the roof and two sidewalls; then the crack regions connect with one another.

As shown in Fig. 8(b), the deformation is first concentrated at the roof (point a), and then destruction points appear at the two sidewalls along the structure plane (points b and c). With continuous vertical loading, the cracks extend from the right and then down the side (point d). Unlike an inclination angle of 0°, hard rock part has almost no deformation during the entire loading process at 30°, indicating that the upper-soft rock withstands the main loading (see Fig. 9(b)). At 0°, the upper-soft rock shifts the load to the lower-hard rock as a load-bearing arch. Because of the different inclination angles, the transmission of the loading force between the soft rock and hard rock are different in local. At 30°, the deformation curves show a stepped increasing as a consequence of the crack development and confined loading.

At an inclination angle of 60° (Fig. 8(c)), an obvious incompatible deformation between the soft rock and hard rock can be observed. As shown in Fig. 9(c), deformation of #3 from the soft rock is larger than #2 from the hard rock during the entire loading. Due to difference in mechanical properties of the mixed strata, the shear zone develops at the structure plane. In soft rock, #1 and #3 have different deformation evolutions. At the beginning of loading, the deformation of #3 is larger than #1. With continuous

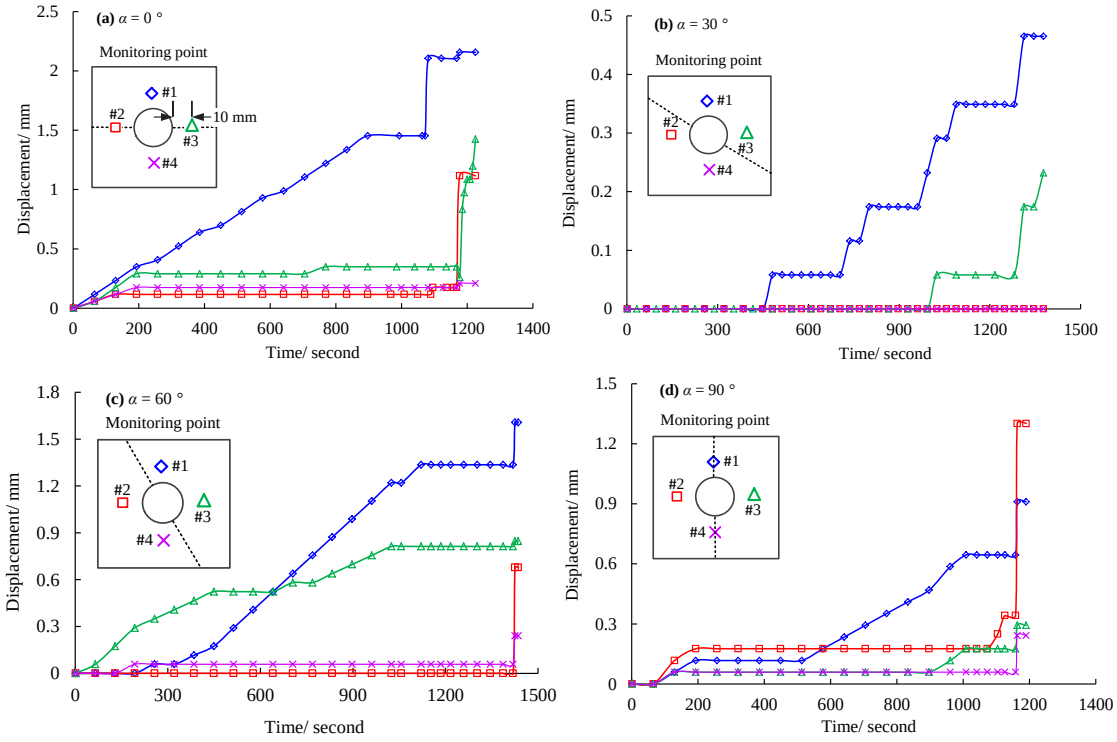

Fig. 9 Comparison of deformations in the surrounding rock

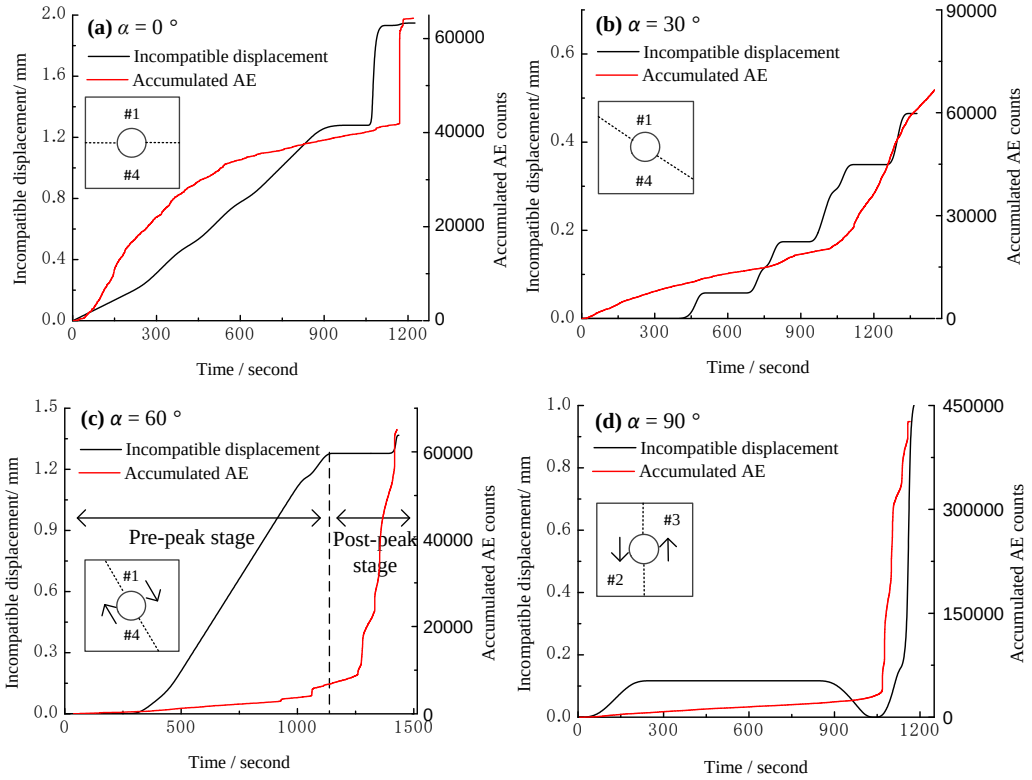

Fig. 10 Effect of incompatible deformations on the damage evolution

vertical loading, the sidewall of the soft rock loses its capacity to withstand, and then the roof begins to slip downward, resulting in the larger deformation of #1. At the post-peak stage, the hard rock experiences split failure and v-shaped notches.

At an inclination angle of 90° (Fig. 8(d)), the deformation of the hard rock dominates the failure process at post-peak stage (point c and d). Unlike other inclination angles, the hard rock at 90° bears the major loads. Incompatible deformation dominated by hard rock can be

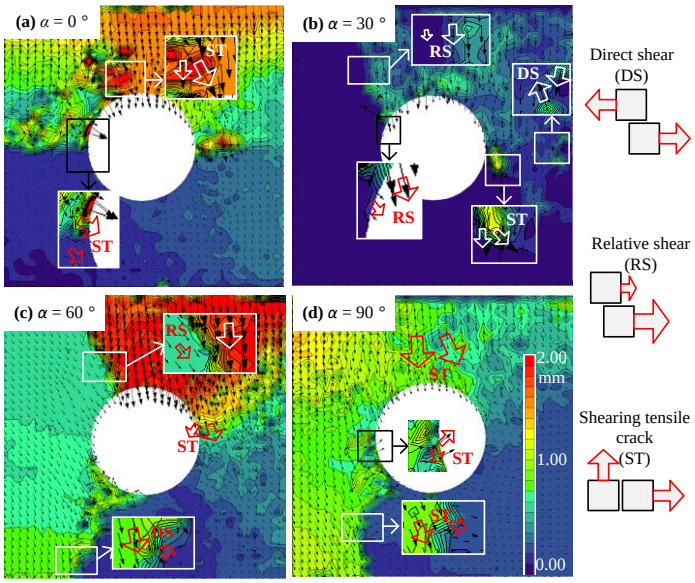

Fig. 11 Displacement field distribution of the final failure by the displacement vectors of the DSCM

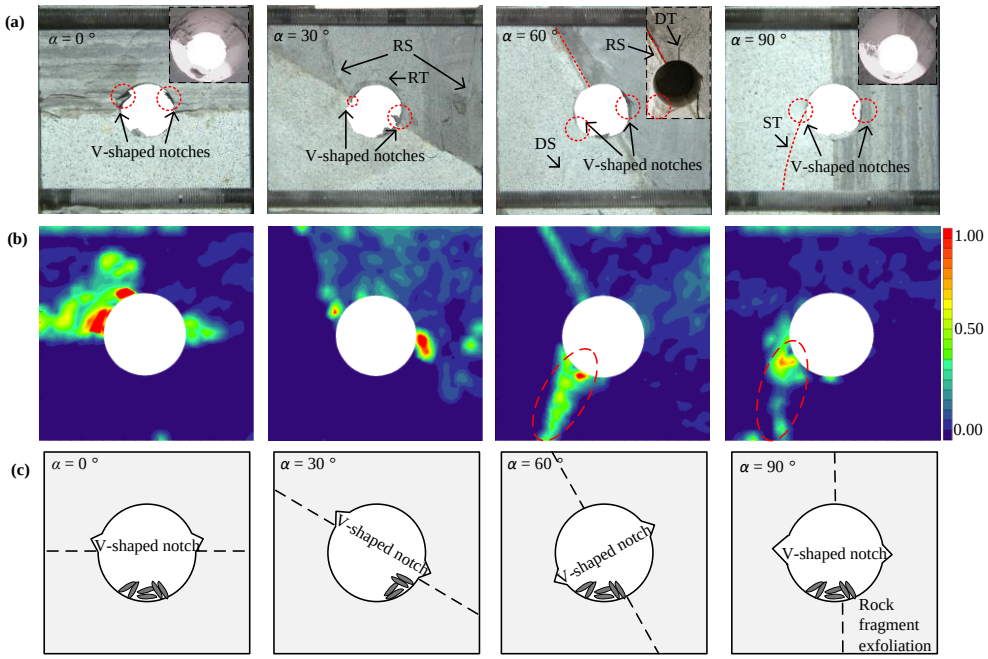

Fig. 12 Final failure mode of the circular tunnels in the mixed strata via experimental tests. (a) Failure image, (b) strain field and (c) schematic diagram of the cracks inside the tunnel

observed in Fig. 9(d), where the deformation of #2 is larger than that of #3, which is different from that of the specimens above.

Incompatible deformation between the soft rock and hard rock controls the failure process, as seen in Fig. 10, where the incompatible deformation value in the curves represents difference between two symmetric monitoring points in the soft rock and hard rock. At inclination angles of 0°, 30° and 90°, incompatible deformations are closely related to the rock damage, which can be quantified using accumulated AE counts. The rock damage is mainly dominated by the soft rock at 0° and 30°, and the hard rock at 90°. However, as seen in Fig. 10(c), incompatible deformations and rock damage are discordant. The incompatible deformation of 60° reaches a maximum with a slow increase at the pre-peak stage, while accumulated AE counts reaches a maximum with a shape increase at the post-peak stage. The reason is due that the soft rock and hard rock alternately bears the major loads during the failure process. Soft rock bears the major loads at the pre-peak stage, while hard rock bears the major loads at post-peak stage.

Through the above analysis of the deformation and failure behaviour, certain findings can be drawn as follows:

When at low inclination angles (0° and 30°), the deformation is controlled by the structure plane. Deformation can no longer expand when it extends to the hardness layer. But the transmission of the loading force

between the soft rock and hard rock are different in local. When at high inclination angles (60° and 90°), the soft and hard rock bear common loads. At 60°, the soft rock dominates the deformation at the pre-peak stage, while hard rock dominates the deformation at post-peak stage. At 90°, the hard rock bears the major loads and dominates the deformation at post-peak stage.

Incompatible deformation between the soft rock and hard rock controls the failure process. At inclination angles of 0°, 30° and 90°, incompatible deformations are closely related to rock damage. At 60°, incompatible deformations and rock damage are discordant due that the soft rock and hard rock alternately bears the major loads during the failure process. The soft rock dominates the deformation at the pre-peak stage, while hard rock dominates the deformation at post-peak stage.

3.3 Final failure mode

Fracture modes represent an important feature for the failure mechanism. Fig. 11 shows the displacement field distribution of the final failure using experimental tests. To better understand the crack type, enlarged views are shown in each displacement field. A crack can be determined by the displacement vectors of the DSCM (Aliabadian *et al*. 2019). Three simplified types of cracks can be summarized as direct shear (DS), relative shear (RS) and shear tensile crack (ST). Direct shear is when the blocks move tangent to the opposite direction. Relative shear is when the blocks move tangent to the same direction but with different displacements. A shear tensile crack is when a block moves tangent (or approximately tangent) to the contact surface and the other moves normal to the contact surface.

At 0°, shear tensile cracks occur at two sidewalls of the soft rock (Fig. 12(a)), which dominate the failure mode. At 30°, shear sliding occurs along the structure plane. Relative shear cracks then dominate the failure mode. At 60°, besides relative shear cracks in soft rock, direct shear crack in hard rock also dominates the failure mode. At 90°, shear tensile cracks mainly occur at the hard rock, showing a typical split mode.

At high inclination angles, the different fracture modes between 60° and 90° could explain why the incompatible deformation of 60° reaches a maximum with a slow increase at the pre-peak stage, while 90° reaches a maximum with a shape increase at the post-peak stage. At 60°, the relative shear crack along the structure plane occurs at pre-peak stage, and the failure of the hard rock leads to the final failure of the entire specimen. At 90°, the split crack of the hard rock dominates the entire failure process.

Fig. 12(b) shows the strain field of the final failure mode for the entire rock specimen. When at low inclination angles (0° and 30°), more strain concentrations are observed in the soft rock layer. This is controlled by the structure plane. When at high inclination angles (60° and 90°), the hard rock experiences more strain concentrations. An obvious shear zone occurs in the hard rock at 60°. At 90°, the hard rock experiences split crack.

As shown in Fig. 12(a) and 12(c), the v-shaped notches develop inside the hole and depend on the inclination angle. When at low inclination angles (0° and 30°), the v-shaped notches are mainly controlled by the structure plane. Progressive spalling failure occurs at the sidewalls along the structure plane in the soft rock. When at high inclination angles (60° and 90°), the v-shaped notches are approximately perpendicular to the structure plane, and the hard rock parts experience more serious damage at final failure.

4. Numerical modelling of the damage evolution

4.1 Numerical model construction

The experimental results clearly reveal the anisotropic mechanical properties and the incompatible deformation. However, the damage evolution of the surrounding rock is difficult to determined using the experimental tests. To further explore the failure mechanism, numerical simulations were performed by FLAC3D (Fast Lagrangian Analysis of a Continua in 3 Dimensions). The basic mechanical parameters used for the simulation are listed in Table 3. The plastic strain ratio represents the equivalent critical plastic strain. The yield ratio and the elastic reduction ratio represent characteristics of the pre-peak and post-peak stages, respectively. As shown in Fig. 13, a damage-softening constitutive model (Yang *et al*. 2019) was used to simulate the internal rock damage.

A good agreement is obtained between the experimental test and numerical results. Comparisons of the uniaxial compressive tests between the experimental test and the numerical simulations are shown in Fig. 14. Though peak strains between the experiment and numerical simulation have gaps, the elastic stages are approximate. This result is probably caused by the impossibility of simulating the rock compaction process through numerical methods. Further, there is a compaction stage exhibiting a concave curve because of the closure of the original micro-cracks at the beginning of the experimental test, which is not observed in the numerical simulations. The loading process and boundary conditions of the numerical model were same as those of the experimental tests.

4.2 Damage evolution and final failure mode

Fig. 15 shows the damage evolution in terms of the per-damage, which represents the degree of damage at every time step. Each specimen has the same trend at the pre-peak stage (Stage I). The increased rates of the models at high inclination angles are higher than those of the models at low inclination angles. Fig. 16 shows the evolution of the damage zone under confined compression. Damage always occurs at sidewalls first and then spreads (step 12000).

At the post-peak stage, low inclination angles (0° and 30°) show different trends with the high inclination angles (60° and 90°), where an obvious platform period (Stage III) occurs at the post-peak stage because the soft and hard rock bear common loads. At low inclination angles (0° and 30°), the damage zones gradually propagate along the structure plane, and then spread to the corners of the model. At Stage III, the damaged areas in the roof connect to the model boundary. The damage area of the soft rock cannot expand

Table 3 Basic mechanical parameters of the simulation model

Lithology	Cohesion (MPa)	Internal friction angle (°)	Elastic modulus (MPa)	Poisson's ratio	Tensile strength (MPa)	Dilation (°)	Plastic strain ratio	Yield ratio	Elastic Reduction Ratio
Soft rock	2.57	34	1.50	0.30	1.48	6	0.040	0.93	0.3
Hard rock	7.92	45	5.97	0.24	3.31	8	0.005	0.99	1.0

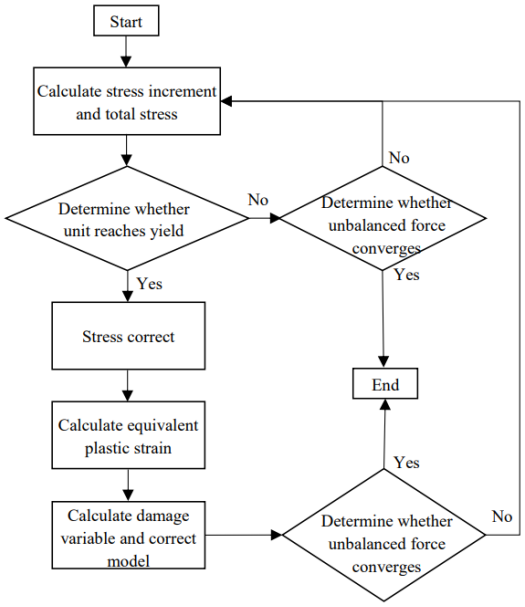

Fig. 13 Damage-softening constitutive model in FLAC3D (Yang *et al*. 2019a)

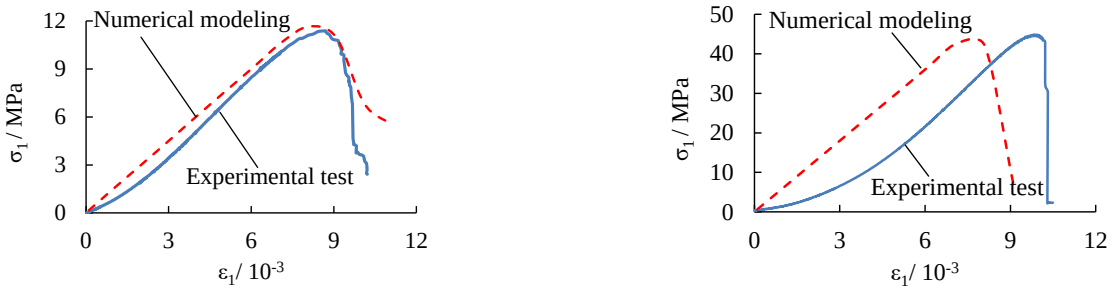

(a) Soft rock (b) Hard rock

Fig. 14 Comparison of the uniaxial compressive tests between the experimental test and numerical modeling

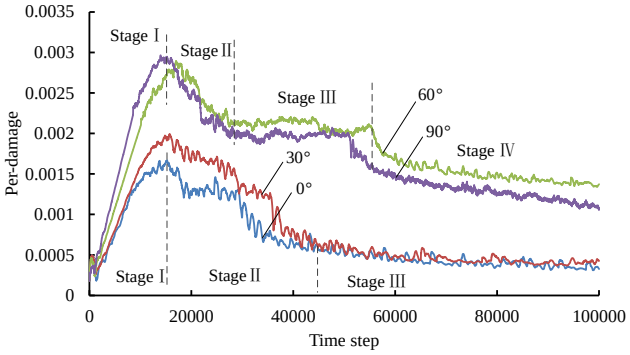

Fig. 15 Damage evolution of the per-damage curves

when it extends to the hard rock, which demonstrates that the structure plane can control the extension of the damage at low inclination angles.

As shown in Fig. 16 by the arrows (step 30000), the damage zones inside the hole show different trends corresponding to the inclination angles. At low inclination angles (0° and 30°), the progressive damage failures occur at the sidewalls along the structure plane in the soft rock, while they are approximately perpendicular to the structure plane at high inclination angles (60° and 90°). At high inclination angles (60° and 90°), the hard rock experiences more damages than the soft rock (step 30000). These trends are in good accordance with the experimental results.

Fig. 17 shows the fractal dimensions of the damage zones with respect to the inclination angle corresponding to the cracks in Fig. 16. The fractal dimensions were calculated by Differential Box-Counting (DBC) method to quantify geometric distribution and fracture characteristics of the damage zones. Differential Box-Counting (DBC) method can be obtained by Eq. (1). The fractal dimension is regard as the degree of damage development to study the

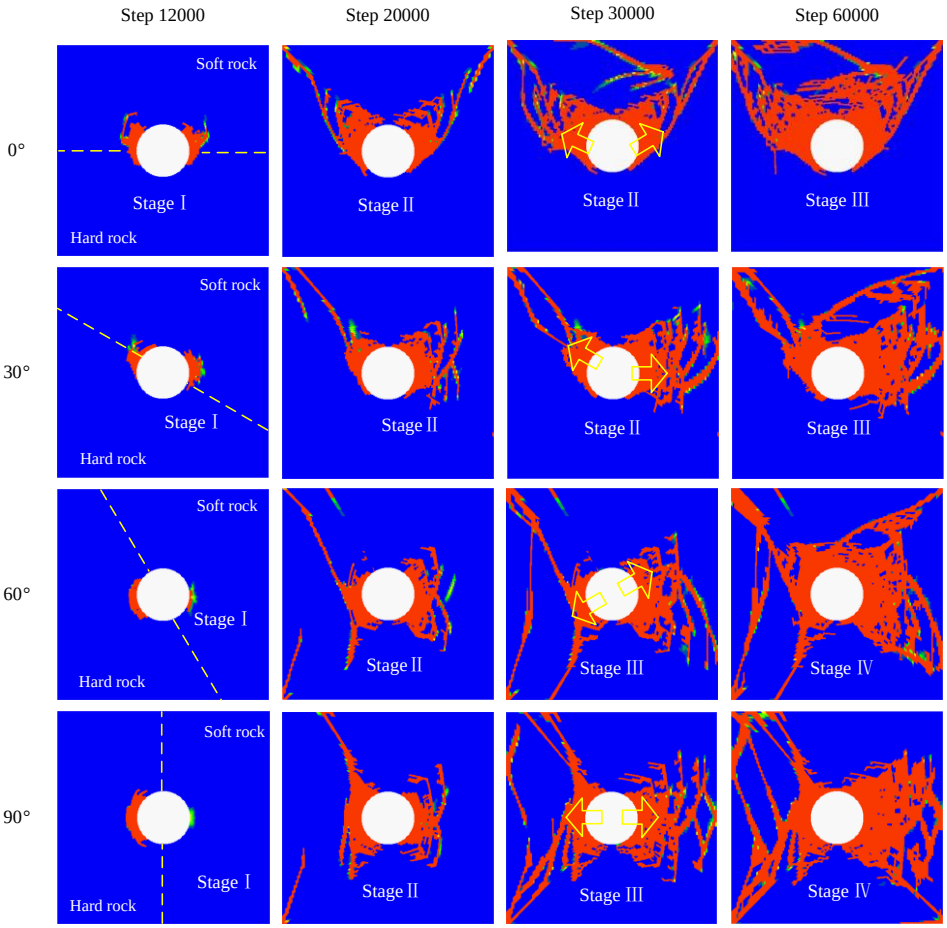

Fig. 16 Evolution of the damage zone under confined compression corresponding to time step in Fig. 15

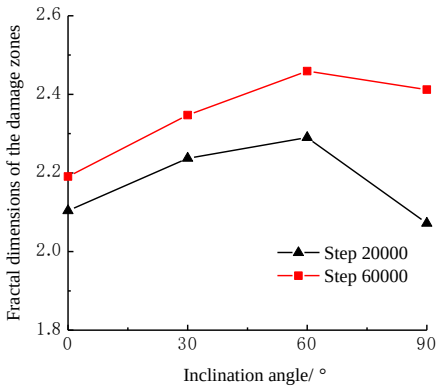

Fig. 17 Fractal dimensions of the damage zones with respect to the inclination angle

damage evolution.

$$\lim_{r\to 0}\frac{\ln N(r)}{\ln\frac{1}{r}} \tag{1}$$

where r is the side length of cube box, D is the fractal box dimension. As the increasing time steps, the fractal dimensions increase with the propagation of cracks. The fractal dimensions first increase reaching a maximum at 60° and then decrease with increasing inclination angles, which indicate that a specimen of 60° has the most complicated fracture characteristics.

Fig. 18 shows the plastic zone of the final failure by numerical simulations, which agrees well with the enlarged views of the cracks observed in the experimental results (Fig. 11). N represents now, and p represents previous in the legend.

As shown in Fig. 19, the ratios of the shear and tensile damage were calculated by the statistical area values of the plastic zone, exhibiting closely relationship between the damage values and inclination angles. As the inclination angles increase, the proportion of shear or tensile damage exhibits a nonlinear increase or decrease, suggesting that

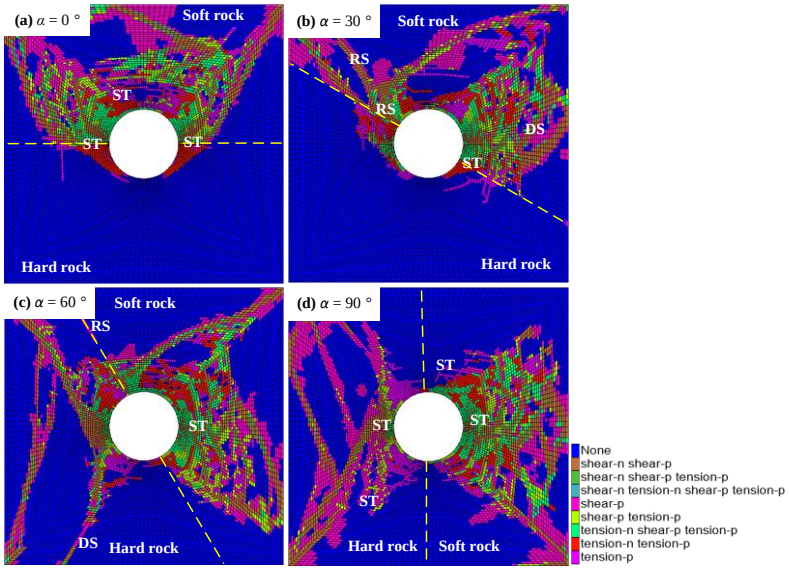

Fig. 18 Plastic zone of the final failure by numerical simulations

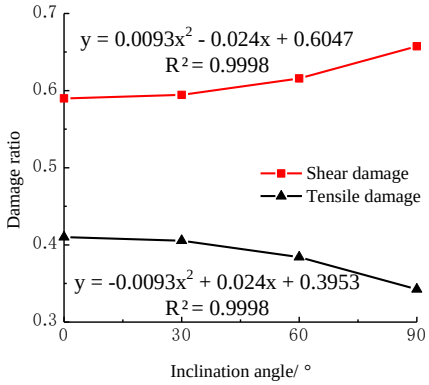

Fig. 19 Damage ratio with respect to the inclination angle

the inclination angle of the mixed strata may promote shear damage and restrain tensile damage. The trends are similar to those of experimental studies by Yang *et al*.(2019b).

5. Conclusions

In this study, confined compression tests were conducted on upper-soft and lower-hard strata specimens using a rock testing system. The incompatible deformation and failure behaviour of the specimens were then analysed based on the DSCM and AE data. Numerical simulations were conducted to explore the damage evolution. The following conclusions can be drawn:

• As the inclination angles increase, the specimens change from ductile failure to brittle failure. Both the strength and deformation of the specimens show the "V" type variations with the strata inclination. The strength anisotropy is greater than the deformation anisotropy.

• When at low inclination angles (0° and 30°), the deformation is controlled by the structure plane. Deformation can no longer expand when it extends to the hardness layer. V-shaped notches inside the hole are also controlled by the structure plane. Progressive spalling failure occurs at the sidewalls along the structure plane in the soft rock. But the transmission of the loading force between the soft rock and hard rock are different in local. When at high inclination angles (60° and 90°), v-shaped notches are approximately perpendicular to the structure plane, and soft and hard rock bear common loads. The hard rock parts experience more serious damage at post-peak stage.

•Incompatible deformation between the soft rock and hard rock controls the failure process. At inclination angles of 0°, 30° and 90°, incompatible deformations are closely related to rock damage. At 60°, incompatible deformations and rock damage are discordant due that the soft rock and hard rock alternately bears the major loads during the failure process.

• The failure trend and modes of the numerical results agree very well with those observed in the experimental results. The fractal dimensions first increase reaching a maximum at 60° and then decrease with increasing inclination angles, which indicate that a specimen of 60° has the most complicated fracture characteristics. As the inclination angles increase, the proportion of the shear or tensile damage exhibits a nonlinear increase or decrease, suggesting that the inclination angle of the mixed strata may

promote shear damage and restrain tensile damage.

Acknowledgments

This research was supported by the National Basic Research Program of China (973 Program) Grant No. 2014CB046905 and the National Natural Science Foundation of China (No.51174197). Additionally, the authors are grateful to the anonymous reviewers of this article for their careful reading of our manuscript and their many helpful comments.

References

Aliabadian, Z., Zhao, G.F., and Russell, A.R. (2019), "Crack development in transversely isotropic sandstone discs subjected to Brazilian tests observed using digital image correlation", *Int. J. Rock Mech. Min. Sci.*, **119**, 211-221. https://doi.org/10.1016/j.ijrmms.2019.04.004

Berčáková, A., Melichar, R. and Souček, K. (2019), "Mechanical properties and failure patterns of migmatized gneiss with metamorphic foliation under UCS test", *Rock Mech. Rock Eng.*, 1-7. https://doi.org/10.1007/s00603-019-02012-2.

Chen, S., Yin, D., Jiang, N., Wang, F. and Zhao, Z. (2019a), "Mechanical properties of oil shale-coal composite samples", *Int. J. Rock Mech. Min. Sci.*, **123**, 104120. https://doi.org/10.1016/j.ijrmms.2019.104120.

Chen, Y., Zuo, J., Liu, D. and Wang, Z. (2019b), "Deformation failure characteristics of coal-rock combined body under uniaxial compression: Experimental and numerical investigations", *Bull. Eng. Geol. Environ.*, **78**(5), 3449-3464. https://doi.org/10.1007/s10064-018-1336-0.

Chen, Z., He, C., Xu, G., Ma, G. and Wu, D. (2019c), "A case study on the asymmetric deformation characteristics and mechanical behavior of deep-buried tunnel in phyllite", *Rock Mech. Rock Eng.*, **52**(11), 4527-4545. https://doi.org/10.1007/s00603-019-01836-2.

Cheng, J.L. (2018), "Study on mechanical behavior of deep composite rock and TBM entrapment prevention and control", Ph.D. Dissertation, China University of Mining and Technology, Xuzhou, China.

Cheng, J.L., Yang, S.Q., Chen, K., Ma, D., Li, F.Y. and Wang, L.M. (2017), "Uniaxial experimental study of the acoustic emission and deformation behavior of composite rock based on 3D digital image correlation (DIC)", *Acta Mechanica Sinica*, **33**(6), 999-1021. https://doi.org/10.1007/s10409-017-0706-3.

Cheng, Z., Pan, W., Li, X. and Sun, W. (2019a), "Numerical simulation on strata behaviours of TCCWF influenced by coal-rock combined body", *Geomech. Eng.*, **19**(3), 269-282. https://doi.org/10.12989/gae.2019.19.3.269.

Cheng, Z., Yang, S., Li, L. and Zhang, L. (2019b), "Support working resistance determined on top-coal caving face based on coal-rock combined body", *Geomech. Eng.*, **19**(3), 255-268. https://doi.org/10.12989/gae.2019.19.3.255.

Cho, J.W., Kim, H., Jeon, S. and Min, K.B. (2012), "Deformation and strength anisotropy of Asan gneiss, Boryeong shale, and Yeoncheon schist", *Int. J. Rock Mech. Min. Sci.*, **50**, 158-169. https://doi.org/ 10.1016/j.ijrmms.2011.12.004.

Dong, W., Song, S., Zhang, B. and Yang, D. (2019), "SIF-based fracture criterion of rock-concrete interface and its application to the prediction of cracking paths in gravity dam", *Eng. Fract. Mech.*, **221**, 106686. https://doi.org/10.1016/j.engfracmech.2019.106686.

Dong, W., Wu, Z., Zhou, X., Wang, N. and Kastiukas, G. (2017), "An experimental study on crack propagation at rock-concrete interface using digital image correlation technique", *Eng. Fract. Mech.*, **171**, 50-63. http://doi.org/10.1016/j.engfracmech.2016.12.003.

Duan, K., Li, Y., Wang, L., Zhao, G. and Wu, W. (2019), "Dynamic responses and failure modes of stratified sedimentary rocks", *Int. J. Rock Mech. Min. Sci.*, **122**, 104060. https://doi.org/10.1016/j.ijrmms.2019.104060.

Dutler, N., Nejati, M., Valley, B., Amann, F. and Molinari, G. (2018), "On the link between fracture toughness, tensile strength, and fracture process zone in anisotropic rocks", *Eng. Fract. Mech.*, **201**, 56-79. https://doi.org/10.1016/j.engfracmech.2018.08.017.

Fortsakis, P., Nikas, K., Marinos, V. and Marinos, P. (2012), "Anisotropic behaviour of stratified rock masses in tunnelling", *Eng. Geol.*, **141**, 74-83. https://doi.org/10.1016/j.enggeo.2012.05.001.

Gong, W., Peng, Y., Sun, X., He, M., Zhao, S., Chen, H. and Xie, T. (2015), "Enhancement of low-contrast thermograms for detecting the stressed tunnel in horizontally stratified rocks", *Int. J. Rock Mech. Min. Sci.*, **74**, 69-80. http://doi.org/10.1016/j.ijrmms.2014.12.002.

Li, A., Dai, F., Xu, N., Gu, G. and Hu, Z. (2019a), "Analysis of a complex flexural toppling failure of large u0nderground caverns in layered rock masses", *Rock Mech. Rock Eng.*, **52**(9), 3157–3181. https://doi.org/10.1007/s00603-019-01760-5.

Li, Y.H., Tang, X.J., Yang, S. and Chen, J. (2019b), "Evolution of the broken rock zone in the mixed ground tunnel based on the DSCM", *Tunn. Undergr. Sp. Technol.*, **84**, 248-258. https://doi.org/10.1016/j.tust.2018.11.017.

Li, Y.H., Zhang, Q., Lin, Z. and Wang, X. (2016), "Spatiotemporal evolution rule of rocks fracture surrounding gob-side roadway with model experiments", *Int. J. Min. Sci. Technol.*, **26**(5), 895-902. https://doi.org/10.1016/j.ijmst.2016.05.031.

Lisjak, A., Garitte, B., Grasselli, G., Müller, H. and Vietor, T. (2015), "The excavation of a circular tunnel in a bedded argillaceous rock (Opalinus Clay): Short-term rock mass response and FDEM numerical analysis", *Tunn. Undergr. Sp. Technol.*, **45**, 227-248. https://doi.org/10.1016/j.tust.2014.09.014.

Liu, R., Huang, N., Jiang, Y., Jing, H. and Yu, L. (2020a), "A numerical study of shear-induced evolutions of geometric and hydraulic properties of self-affine rough-walled rock fractures", *Int. J. Rock Mech. Min. Sci.*, **127**, 104211. https://doi.org/10.1016/j.ijrmms.2020.104211.

Liu, R., Wang, C., Li, B., Jiang, Y. and Jing, H. (2020b), "Modeling linear and nonlinear fluid flow through sheared rough-walled joints taking into account boundary stiffness", *Comput. Geotech.*, **120**, 103452. https://doi.org/10.1016/j.compgeo.2020.103452.

Martin, C.D. (1997), "Seventeenth Canadian geotechnical colloquium: the effect of cohesion loss and stress path on brittle rock strength", *Can. Geotech. J.*, **34**(5), 698-725. https://doi.org/10.1139/t97-030.

Meng, Z., Lu, P. and He, X. (2009), "Depositinonal structure planes and their influence on the mechanical properties of sedimentary rock mass", *Coal Geol. Explor.*, **37**(1), 33-37.

Mezger, F., Ramoni, M., Anagnostou, G., Dimitrakopoulos, A. and Meystre, N. (2017), "Evaluation of higher capacity segmental lining systems when tunnelling in squeezing rock", *Tunn. Undergr. Sp. Technol.*, **65**, 200-214. https://doi.org/10.1016/j.tust.2017.02.012.

Selçuk, L. and Aşma, D. (2019), "Experimental investigation of the rock-concrete bi materials influence of inclined interface on strength and failure behavior", *Int. J. Rock Mech. Min. Sci.*, **123**, 104119. https://doi.org/10.1016/j.ijrmms.2019.104119.

Tien, Y.M., Kuo, M.C. and Juang, C.H. (2006), "An experimental

investigation of the failure mechanism of simulated transversely isotropic rocks", *Int. J. Rock Mech. Min. Sci.*, **43**(8), 1163-1181. https://doi.org/10.1016/j.ijrmms.2006.03.011.

Tóth, Á., Gong, Q. and Zhao, J. (2013), "Case studies of TBM tunneling performance in rock-soil interface mixed ground", *Tunn. Undergr. Sp. Technol.*, **38**, 140-150. https://doi.org/10.1016/j.tust.2013.06.001.

Wang, D.J., Tang, H., Shen, P., Su, X. and Huang, L. (2019a), "Co-effects of bedding planes and parallel flaws on fracture evolution in anisotropic rocks", *Eng. Geol.*, **264**, 105382. https://doi.org/10.1016/j.enggeo.2019.105382.

Wang, S., Sloan, S., Tang, C. and Zhu, W. (2012), "Numerical simulation of the failure mechanism of circular tunnels in transversely isotropic rock masses", *Tunn. Undergr. Sp. Technol.*, **32**, 231-244. https://doi.org/10.1016/j.tust.2012.07.003.

Wang, Y., Tan, W., Liu, D., Hou, Z. and Li, C. (2019b), "On anisotropic fracture evolution and energy mechanism during marble failure under uniaxial deformation", *Rock Mech. Rock Eng.*, **52**(10), 3567-3583. https://doi.org/10.1007/s00603-019-01829-1.

Yang, S.Q., Chen, M., Fang, G., Wang, Y.C., Meng, B., Li, Y.H. and Jing, H.W. (2018), "Physical experiment and numerical modelling of tunnel excavation in slanted upper-soft and lower-hard strata", *Tunn. Undergr. Sp. Technol.*, **82**, 248-264. https://doi.org/10.1016/j.tust.2018.08.049.

Yang, S.Q., Hu, B. and Xu, P. (2019a), "Study on the damage-softening constitutive model of rock and experimental verification", *Acta Mechanica Sinica*, **35**(4), 786-798. https://doi.org/10.1007/s10409-018-00833-y.

Yang, S.Q., Yin, P.F., Huang, Y.H. and Cheng, J.L. (2019b), "Strength, deformability and X-ray micro-CT observations of transversely isotropic composite rock under different confining pressures", *Eng. Fract. Mech.*, **214**, 1-20. https://doi.org/10.1016/j.engfracmech.2019.04.030.

Zang, C.W., Chen, M., Zhang, G.C., Wang, K. and Gu, D.D. (2020), "Research on the failure process and stability control technology in a deep roadway: numerical simulation and field test", *Energy Sci. Eng.*, 1-14. https://doi.org/10.1002/ese3.664.

Zhang, G., Ranjith, P.G., Wu, B., Perera, M.S.A., Haque, A. and Li, D. (2019c), "Synchrotron X-ray tomographic characterization of microstructural evolution in coal due to supercritical CO_2 injection at in-situ conditions", *Fuel*, **255**, 115696. https://doi.org/10.1016/j.fuel.2019.115696.

Zhang, G., Ranjith, P.G., Liang, W., Haque, A., Perera, M.S.A. and Li, D. (2019a), "Stress-dependent fracture porosity and permeability of fractured coal: An in-situ X-ray tomography study", *Int. J. Coal Geol.*, **213**, 103279. https://doi.org/10.1016/j.coal.2019.103279.

Zhang, G., Ranjith, P.G., Perera, M.S.A., Lu, Y. and Choi, X. (2019b), "Quantitative analysis of micro-structural changes in a bituminous coal after exposure to supercritical CO_2 and water", *Nat. Resour. Res.*, **28**(4), 1639-1660. https://doi.org/10.1007/s11053-019-09463-y.

Zhong, H., Ooi, E.T., Song, C., Ding, T., Lin, G. and Li, H. (2014), "Experimental and numerical study of the dependency of interface fracture in concrete-rock specimens on mode mixity", *Eng. Fract. Mech.*, **124**, 287-309. https://doi.org/10.1016/j.engfracmech.2014.04.030.